Proceedings of ASME Turbo Expo 2024
Turbomachinery Technical Conference and Exposition
GT2024
June 24-28, 2024, London, United Kingdom

GT2024-123825

INSIGHTS INTO TURBOCHARGER CENTRIFUGAL COMPRESSOR STABILITY USING HIGH-FIDELITY CFD AND A NOVEL IMPELLER DIFFUSION FACTOR

Yiming Liu[1], Stephen Spence[1], John Horsley[2], Stuart Mann[2], Charles Stuart[1]

[1]Trinity College Dublin, Dublin, Ireland
[2]Cummins Engine Components, Huddersfield, UK

ABSTRACT

Turbocharger technologies are widely applied in the modern automotive industry to meet increasingly stringent carbon emission standards. To support the continuous enhancement of these tactics, delivering improvement to the performance and stability of turbocharger compressors at low mass flow rate regimes is of paramount importance.

The present paper investigated the stability of a turbocharger compressor stage equipped with a ported shroud, using high-fidelity CFD simulations. It was found that the recirculated flow passing through the ported shroud device had primary influence on the flow condition in the vicinity of the impeller tip region (80% to 100% span). This discovery facilitated the definition of a modified impeller diffusion factor (DF), which was applied to the CFD results for three different compressor geometry configurations to lead to the provision of quantitative metrics for impeller stability. Furthermore, the observed change in the limiting impeller DF along the compressor surge line indicated that the dominant components governing the instability of the entire stage had switched, i.e., the stalling behavior of the compressor stage had transitioned from impeller dominated stall to vaneless diffuser dominated stall. Additionally, the limiting impeller DF clearly showed that one of the compressor configurations with a change in the hub endwall recess around the rear of the impeller improved the impeller stability by 3%. By comparison, another configuration with a change to strut geometry in the ported shroud recirculation channel reduced the impeller stability by 10%.

The present work addressed the gap in the understanding about the stability of different compressor configurations equipped with a ported shroud, and was useful for determining the changes in compressor global and local instability through a quantitative parameter based on a modified definition of DF.

Keywords: Turbocharger Compressor; Stability; Impeller Diffusion Factor; CFD; Ported Shroud

NOMENCLATURE

Symbols

b	=	diffuser width (m)
CV	=	coefficient of variance
c	=	absolute velocity (m/s)
DF	=	impeller diffusion factor
L	=	blade length (m)
Ma	=	Mach number in absolute frame
MFP	=	mass flow parameter ($m \cdot s \cdot K^{1/2}$)
$\dot{m}$	=	corrected mass flow rate (kg/s)
p	=	static pressure (Pa)
Δp	=	inlet pressure differential (Pa)
RR	=	recirculation ratio
r	=	radius (m)
s_g	=	specific entropy generation rate ($m^2 \cdot s^{-3} \cdot K^{-1}$)
u	=	peripheral velocity (m/s)
w	=	relative velocity (m/s)
Z	=	blade number
η	=	stage isentropic efficiency
μ	=	mean value
σ	=	standard deviation
ϕ	=	flow coefficient

Abbreviation

B	=	baseline configuration
BPF	=	blade passing frequency
CFD	=	computational fluid dynamics
EXP	=	experiment
GCI	=	grid convergence index
M	=	million; modified struts configuration
MWE	=	map width enhancement

PSD	=	power spectrum density
R	=	enlarged diffuser recess configuration
SST	=	shear stress transport

Subscripts

00	=	throat of the converging nozzle for flow measurement upstream of the compressor
0	=	bellmouth throat
1	=	main blade leading edge
2	=	impeller outlet
3	=	diffuser outlet
5	=	stage outlet in experiment
a	=	axial component
atm	=	atmosphere
E	=	exducer
h	=	hub
I	=	inducer
rms	=	root mean square
s	=	shroud
t	=	total
tip	=	blade tip
u	=	peripheral component

1. INTRODUCTION

As global concerns over greenhouse gases grow, engine manufacturers are under pressure to reduce carbon emissions from their products. By facilitating enhanced engine power density, turbochargers have emerged as one of the key technologies to reduce CO_2 emissions. The success of turbocharging systems is highly dependent on the performance and stability of the centrifugal compressor stage. Especially when combined with complementary technologies such as Miller valve timing, the result is an ongoing need for improvements to the performance and stability of the turbocharger compressor at low flow rate operating conditions [1].

A number of approaches have been adopted in an attempt to enhance compressor stability at low flow rates. One of the most popular map width enhancement (MWE) techniques in turbocharging industry is the inducer recirculating bypass system, which is also known as a shroud bleed slot system, ring groove arrangement or ported shroud insert. The ported shroud insert helps improve surge margin by recirculating low-momentum flow near the inducer shroud when operating close to surge. Additionally, when operating towards the choke side of the performance map, the flow direction through the ported shroud reverses and provides a means of bypassing the impeller throat when it is choked, thus offering the potential to increase the compressor maximum flow capacity. A typical turbocharger compressor equipped with a ported shroud is shown in Figure 1.

Since Fisher [2] introduced the ported shroud in the late 1980s, many studies have been launched on it. Sivagnanasundaram et al. [3] investigated the impact of inducer bleed slot geometry variations on the enhancement of the compressor map width. It was found that increasing the width of

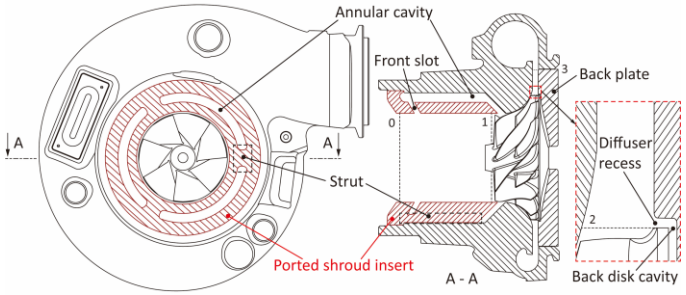

Figure 1: Schematic of turbocharger compressor geometry

inducer bleed slot was beneficial to widen the compressor map to lower flow rate regions, but with an adverse effect on efficiency. The research [4] was also extended to adding vanes into the annular bleed cavity. Results showed that an effective vane design can enhance guidance of the recirculated flow within the annular bleed cavity and further enhance the compressor stability at small flow rates without causing efficiency penalties. A series of studies were conducted by Tamaki and Zheng et al. [5][6][7] on different shapes of the ported shroud slot. It was pointed out that the circumferential distortion caused by the volute tongue propagated upstream, inducing an asymmetrical flow field at the impeller inducer. This non-uniform flow disturbance can be compensated by adopting a non-axisymmetric sinusoidal-shaped bleed slot. Comparing with a traditional axisymmetric bleed slot, the novel non-axisymmetric bleed slot demonstrated a greater potential for stability enhancement, but increased manufacturing complexity.

The fundamental mechanisms by which a ported shroud enhances the stability of a compressor have also been explored. It is generally considered that, at low flow rates, the ported shroud removes the low-momentum recirculating flow near the inducer tip region and recirculates it back upstream of the leading edge which increases the axial velocity at inlet and reduces the inducer incidence angle. He et al. [8] conducted experiments to show that the ported shroud removed the vortical structures present in the vicinity of the inducer tip to effectively eliminate rotating instability and stall at low impeller speeds. Moreover, the ported shroud was shown to elevate impeller input work and change the pressure rise characteristics of the impeller and diffuser, thereby suppressing the onset of surge of the compressor system at middle and high impeller speeds. Guillou et al. [9] applied particle image velocimetry (PIV) technology and dynamic pressure transducers to analyze the relationship between inducer tip recirculation flow and compressor instability behaviors, and reached similar conclusions.

The stability of a turbocharger compressor near surge can also be affected by the size and the position of the diffuser recess. The diffuser recess refers to a groove structure formed where the impeller back disk cavity connects to the diffuser hub, as shown in Figure 1. Nikpour [10] clearly illustrated that a change in the diffuser recess shape created different recirculation areas at the impeller blade trailing edge, which acted as an aerodynamic

pinch and had a profound impact on the compressor stability. Spakovszky and Roduner [11] studied a bleed air system on the hub side between the impeller and diffuser, which can also provide some insights into the interaction of the mainstream flow and secondary flow induced by the existence of back disk cavity.

Many of the studies have focused on the stability enhancement brought by inclusion of a ported shroud in comparison to a compressor stage with smooth casing. However, few studies have explored the impact of different ported shroud geometries on compressor stage stability. In other words, while the benefits of introducing a ported shroud have been well studied, the impacts of its variations on stage stability remain relatively unexplored. Chen et al. [12] and Tamaki [13] investigated the impact of various ported shroud geometry configurations on compressor map width, but these studies based on 1D analysis and steady-state CFD simulations utilizing a simplified model provided limited insights into the underlying flow mechanisms. Additionally, there has been little research into the changes in compressor stability caused by various diffuser recess locations and sizes.

The present paper reports a stability study on a ported shroud equipped turbocharger compressor stage with various geometry configurations. On the basis of stage performance data obtained through experimental measurements, key flow phenomena pertaining to each geometry configuration were revealed using high-fidelity unsteady CFD simulations. Then, the ported shroud insert was analyzed in terms of its recirculated mass flow rate and the pre-swirl condition that it introduced at compressor inlet, and the guidance was provided for improving the definition of impeller diffusion factor in this context and its evaluation method. Finally, the stability limit of the impeller was assessed based on the modified impeller diffusion factor, and the switch over of compressor instability modes was explained according to the surge boundary of the experimentally measured compressor stage performance map.

2. GEOMETRY AND EXPERIMENTAL RESULTS

2.1 Geometry

The investigated turbocharger centrifugal compressor stage was for a heavy-duty diesel application, provided by Cummins Engine Components. The compressor stage comprised of a ported shroud insert, an unshrouded impeller with seven main blades and seven splitter blades, a vaneless diffuser and a volute. The ported shroud insert had three struts to connect its inner part and outer part. The three struts were spaced in the circumferential direction, to create an annular bleed cavity as shown in Figure 1. To preserve the proprietary nature of the geometry, the illustrations presented in Figure 1 are schematic in nature and not to scale. Some main parameters of the compressor stage are summarized in Table 1.

Three different compressor variations were investigated, all of which had a ported shroud. The initial configuration of the compressor stage was named as the baseline configuration (B). Two additional geometry configurations of the compressor stage were investigated. One configuration had a change in the ported shroud configuration which reduced the axial extent of the supporting struts; this was named as the (M) configuration. The other configuration had an enlarged diffuser recess around the impeller outlet combined with the original baseline ported shroud arrangement; this was named as the (R) configuration.

Table 1: Compressor stage dimensions

b_2/r_2	$r_{1,s}/r_2$	$r_{1,h}/r_2$	r_3/r_2
0.124	0.708	0.199	1.538

2.2 Stage Performance

The stage performance maps of all three geometry configurations were measured at the test facilities of Cummins Engine Components. Figure 2 shows the layout of the test rig. The experimental measurements were conducted on a two-loop hot gas test stand in accordance with SAE J1826-Turbocharger Gas Stand Test Code [14]. A main air control valve downstream of a pressurized air supply was used to control the mass flow through the turbine and thus the speed of the turbine and the compressor. Turbine inlet temperature was maintained at a constant value throughout the test campaign. The compressor was throttled towards surge along each speedline by closing the boost valve.

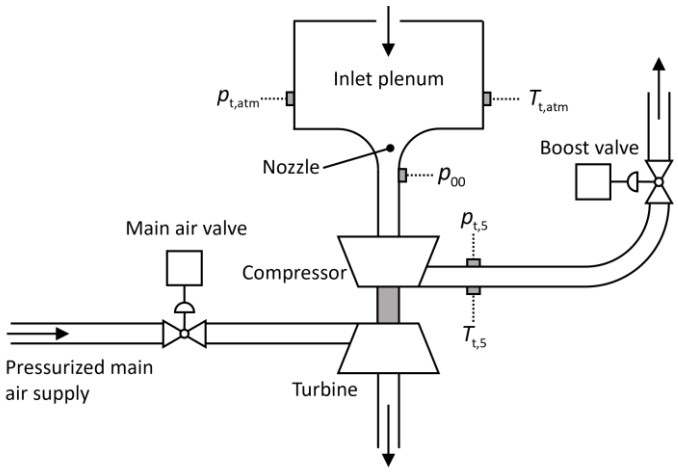

Figure 2: Schematic of test rig layout

The total pressure ratio of the stage was defined as the ratio of $p_{t,5}$ to $p_{t,atm}$. The flow rate was calculated by taking the inlet differential pressure measurement Δp from the total pressure in the inlet plenum to the static pressure at the throat of the nozzle:

$$\Delta p = p_{t,atm} - p_{00} \quad (1)$$

The inlet differential pressure was also used to detect if surge occurred. The differential pressure transducer located between the inlet plenum and the nozzle throat could detect the fluctuation of inlet pressure, which was indicative of the inception of surge. The coefficient of variance (CV) of this inlet differential pressure Δp was adopted to determine if the compressor was in surge according to Equation 2:

$$CV = \frac{\sigma(\Delta p)}{\mu(\Delta p)} \times 100\% \quad (2)$$

where σ indicates the standard deviation, and μ implies the mean value. *CV* was calculated using a rolling 50 data, at a frequency of 25 Hz. Once the *CV* value of Δp increased beyond a preset threshold, then surge was considered to occur. The flow rate logged at this time was deemed as the surge flow rate of the tested turbocharger compressor stage.

To obtain the inlet differential pressure Δp, two kinds of pressure transducers were used. For flow rate measurement, a Honeywell PPT 0100 differential pressure transducer was adopted, since it can provide a precise and stable measurement with an accuracy of ±0.05% of the full scale. For surge detection measurement, a UNIK 5000 differential pressure transducer was employed, which had a higher response frequency of 3.5 kHz with an uncertainty of ±0.2% of the full scale. More details of the test rig arrangements and surge measurement can be found in the previous study published by Cummins Engine Components [15].

Figure 3 shows the total pressure ratio measurements of the three geometry configurations along five speedlines. The mass flow parameter (*MFP*) values are normalized to the choke value of the 100% speedline. The surge limit for each configuration is specified by a dashed line. It can be seen that different geometry configurations had a profound impact on the compressor surge flow rate. The modified diffuser recess R configuration improved the compressor stability and reduced the surge flow rate, whereas modified struts M configuration pushed the surge boundary to higher flow rates. The changes in geometry configurations had no significant influence on the maximum choke flow rates.

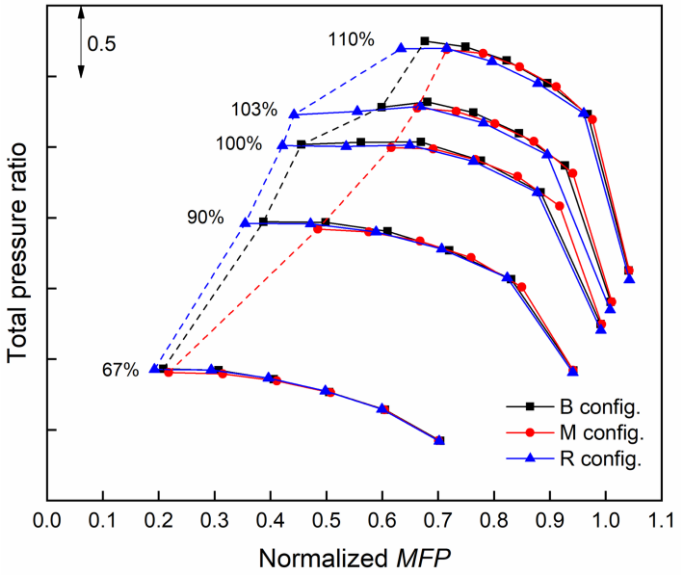

Figure 3: Experimental measurements of compressor stage performance map

3. NUMERICAL METHOD

Considering the circumferential non-uniformity induced by the volute tongue and the struts of the ported shroud, a full-annulus numerical model was established and simulated in this study. The numerical model of the baseline B configuration is shown in Figure 4. It consisted of two stationary domains (ported shroud insert domain and volute domain), and one rotating domain (impeller domain). The inlet and outlet ducts were extended to six times the radius of the inlet and outlet, respectively, to avoid recirculating flow crossing the system boundaries and, consequently, to enhance the uniformity at the stage performance measurement planes in the numerical simulations [16]. Geometric details such as the blade root fillets, and back disk cavity were included to replicate the experimentally tested compressor stages as accurately as possible.

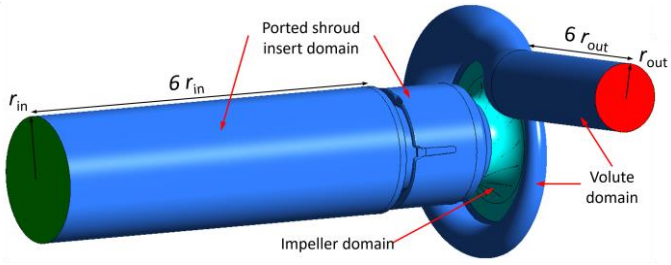

Figure 4: CFD model of the baseline B configuration

Figure 5 illustrates the meridional view of the computational domain of the baseline B configuration. Domain interfaces were carefully defined to avoid locating them within regions of recirculating flow, in anticipation of not affecting the internal flow field of the impeller and vaneless diffuser. All interfaces were configured using the "frozen rotor" option in steady simulations, and "transient rotor stator" in unsteady simulations. The rotating impeller domain contained not only the impeller passages, but also the vaneless diffuser, back disk cavity and part of the ported shroud channel extending from the bleed slot in the shroud. Impeller shroud, extension channel, diffuser walls and back plate were set as counter rotating (blue lines in Figure 5), so that they performed as stationary walls in the stationary frame of reference. All solid walls were set as being smooth in the model except for the volute wall, which had an equivalent sand grain roughness of 32 μm (green line in Figure 5). Non-slip adiabatic conditions were adopted on all solid walls.

Numerical simulations were performed by solving the 3D compressible Reynolds-averaged Navier-Stokes (RANS) equations using the commercial software Ansys CFX 2021R1. The shear stress transport *k-ω* (SST *k-ω*) turbulence model with reattachment modification activated was employed for turbulence term closure due to the improved flow field predictions near stall compared with the standard SST *k-ω* model and other commonly used turbulence models [17]. The boundary conditions at stage inlet were assigned a total pressure of 101325 Pa, a total temperature of 288.15 K, and flow direction normal to the boundary. A static pressure boundary condition was specified at stage outlet when the flow condition was near choke; mass flow rate was used as the outlet boundary condition at other flow conditions. Steady simulations were conducted for three operating points near the choke limit on each speedline. Unsteady (URANS) simulations were performed for the other

three operating points close to the surge limit. Instantaneous results from the last timestep of these unsteady simulated operating points were given in this study.

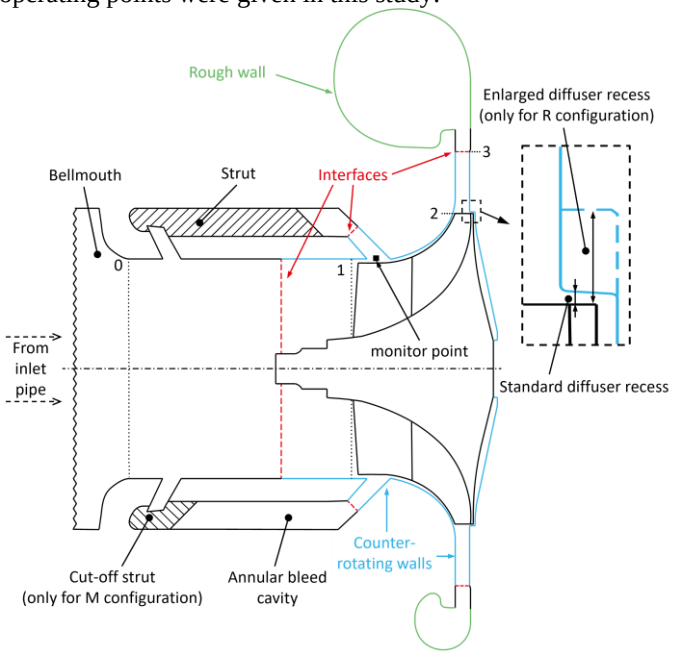

Figure 5: Meridional view of the baseline B configuration

A fully structured hexahedral grid was generated using Ansys ICEM for the impeller domain to reduce numerical diffusion and improve accuracy in the impeller and the diffuser. The grids for the other two stationary domains were unstructured and were generated by Ansys ICEM. To meet conditions for using SST *k-ω* model, the height of the first cell adjacent to the solid wall was set to be 0.002 mm, so that 99.5% of the blade surface had a dimensionless distance y^+ less than 2 at the peak efficiency operating condition on the 100% speedline (operating point P shown in Figure 6). Grid independence study was conducted for all three domains to ensure the CFD solutions were grid independent for each domain. The grid convergence index (GCI) [18] was employed to evaluate the discretization error of the generated grids. The GCI study results are given in Figure 6 to show the effect of impeller domain grid number of the baseline B configuration on stage isentropic efficiency at 100% speed (i.e., B_100%). It is noted that the infinite grid (dashed line) is a hypothetical result. The result of the infinite grid was generated through the application of Richardson extrapolation [19] to the results of coarse, medium and fine grids, and can be considered as the reference for a solution exhibiting zero discretization error. All simulations undertaken as part of the process of evaluating grid independence were steady-state. Results for S1 condition were not given due to convergence limitations of steady simulations.

Table 2 summarizes the results of the grid independence study for one impeller passage. The numerical errors were averaged by all simulated points over the whole speedline, and compared with experimental data and infinite grid references, respectively. The simulation time was normalized by the time running the medium size grid case on an Intel Xeon E5-2690 v3 computer using 20 cores. Considering the balance between numerical accuracy and computational efficiency, the medium size grid was chosen for the following study. The same procedure was performed for the ported shroud insert domain grid and volute domain grid, however the results are not shown here for the sake of brevity. The final grid size for the baseline configuration was 15.5 million nodes in total, as summarised in Table 3. The unsteady simulation results with the medium size grid were also added to Figure 6, which successfully represented the entirety of the experimentally measured stable operating range. The grid size for the other two configurations has been slightly adjusted to accommodate the geometry alterations associated with the struts change and diffuser recess change.

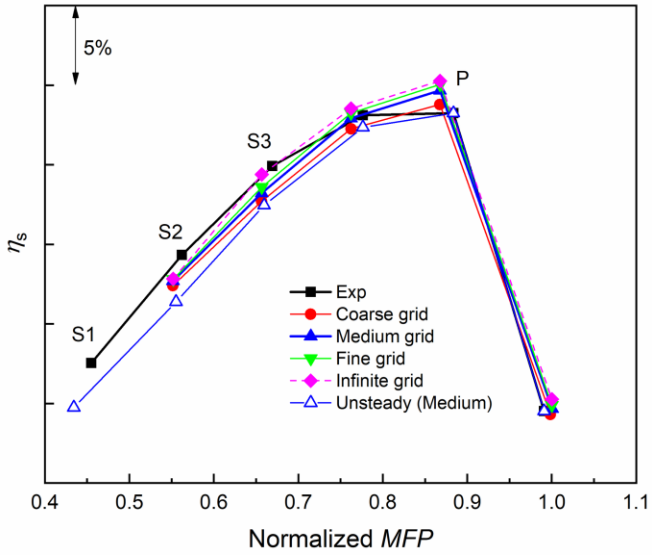

Figure 6: Grid independence check results

Table 2: Grid independence results for one impeller passage

	Nodes	Numerical error		Normalized CFD time
		to EXP	to infinite gird	
Coarse	0.9 M	1.68%	1.59%	0.57
Medium	1.8 M	1.10%	0.85%	1.00
Fine	3.5 M	0.87%	0.47%	1.70

Table 3: Grid information of the baseline B configuration

	Ported shroud	Impeller	Volute	Total
Nodes	1.7 M	12.3 M	1.5 M	15.5 M
Elements	4.7 M	11.9 M	3.9 M	20.5 M
Type	Unstruct.	Structured	Unstruct.	

A systematic timescale independence study was conducted at the S1 condition (see Figure 6), which was the last experimentally measured stable operating point on the 100% speedline. Figure 7(a) records the static pressure histories from a monitor point located at the interface between the downstream flow of the ported shroud and the compressor housing shroud contour (denoted by the square in Figure 5) at different timescales. The abscissa denotes the dimensionless time taken

for the impeller to rotate through the angle subtended by one main blade passage. Additionally, the power spectrum density (PSD) [20] of the pressure fluctuations were estimated by Welch's method for frequency comparison and shown in Figure 7(b). The results indicated that 60 timesteps per main blade passing period was sufficient both in terms of pressure signal traces and frequencies. The number of sub-iteration within each timestep was five in this study.

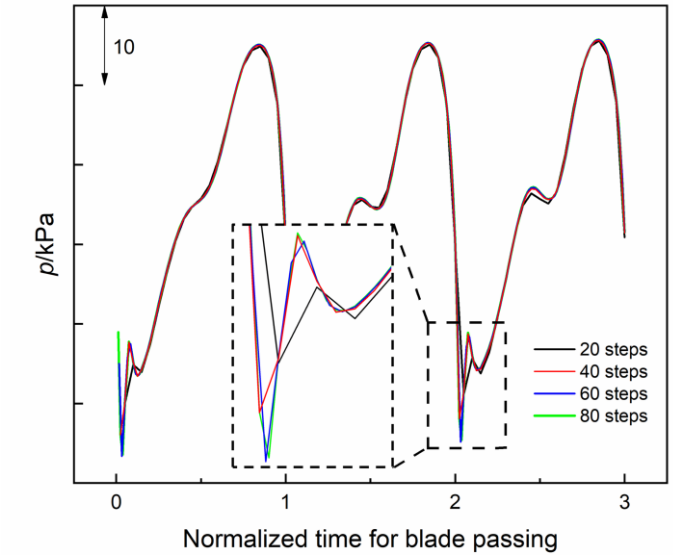

(a) Pressure history

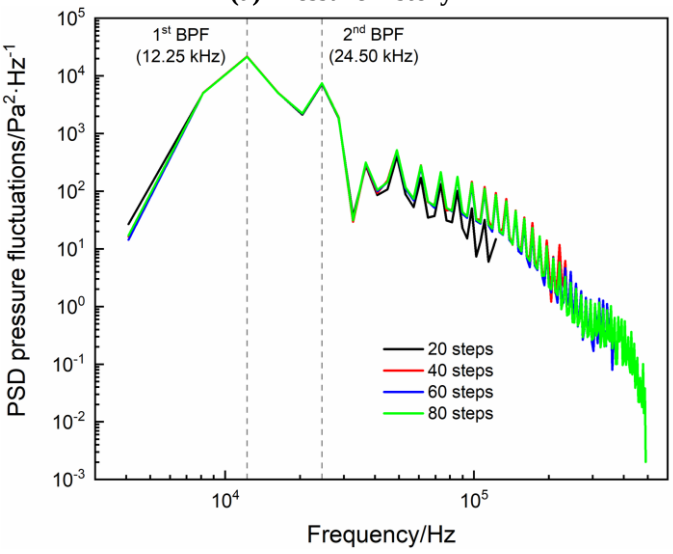

(b) PSD results for pressure fluctuations

Figure 7: Timescale independence check results

4. PRELIMINARY ANALYSIS OF COMPRESSOR STAGE STABILITY

4.1 Ported Shroud Performance

Different from the traditional compressor stage with a smooth shroud wall and no bleed slot, the ported shroud provides additional mass flow to the impeller and thus changes the flow field of the impeller. Therefore, the performance of the ported shroud was analyzed to facilitate the subsequent investigations of impeller flow field and compressor stage stability. A parameter termed recirculation ratio (*RR*) was defined as the difference between mass flow rate at impeller inlet and stage inlet, non-dimensionalized by the stage mass flow rate:

$$RR = \frac{\dot{m}_1 - \dot{m}_0}{\dot{m}_0} \tag{3}$$

where the subscript 0 denotes the bellmouth throat location upstream of the ported shroud recirculation slot and subscript 1 is just upstream of the main blade leading edge, as shown in Figure 5. Stage flow coefficient ϕ was used to normalize *RR*, which has the definition:

$$\phi = \frac{c_{0,a}}{u_{1,tip}} \tag{4}$$

where $c_{0,a}$ indicates the axial velocity at the bellmouth throat, and $u_{1,tip}$ is the tip peripheral velocity of main blade leading edge.

Figure 8 shows the recirculation ratio characteristic of the ported shroud. The positive data indicated that the ported shroud recirculated low-momentum flow from inducer shroud to impeller inlet, and the negative data implied that the ported shroud acted as a bypass around the inducer throat. All data observations from different geometry configurations at different speeds were almost perfectly distributed along a quartic curve with R^2 over 0.99. This means the recirculation capacity of the ported shroud was a function of the stage inlet flow coefficient, but was unaffected by the impeller speed or the various geometry configurations considered here. Changing the strut geometry within the ported shroud had no influence on recirculation/bypass flow rate.

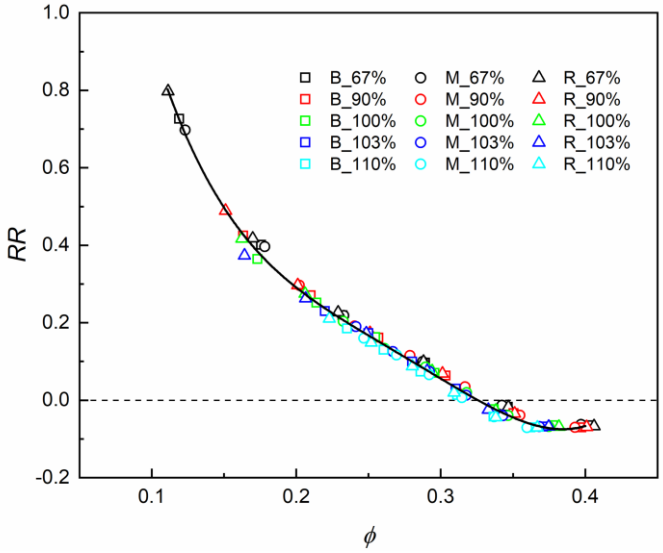

Figure 8: Characteristic of ported shroud recirculation ratio performance

Figure 9 shows the absolute instantaneous Mach number overlaid with flow vectors in ported shroud cavity for the baseline B configuration and the modified struts M configuration. The operating condition was at a normalized *MFP* of 0.62 on the 100% speedline, which corresponded to the

minimum stable flow rate of modified struts M configuration at 100% speed. The radius of the revolution surface is 136% of $r_{1,s}$, which is approximately the mid-span within the ported shroud cavity. The red dashed boxes indicate the upstream slot of the ported shroud where recirculated flow enters the mainstream upstream of the impeller leading edge. The recirculated flow from the inducer shroud had a swirl component in the same direction as the impeller rotation. The struts in the baseline B configuration had a significant de-swirling effect, and even reversed the direction of the swirl due to a large recirculating region forming on one side of each strut, as evident in Figure 9(a). For the modified struts M configuration, the reduced axial extent of the struts limited the blockage effect on the recirculated flow, thus the recirculated flow entering the main flow retained the original swirl direction and most of the swirl magnitude.

4.2 Influence of Recirculated Flow on Impeller

The differences in the flow field within the ported shroud cavity resulted in different pre-swirl flow conditions at impeller inlet. Figure 10 compares the circumferential absolute velocity on a plane 10 mm upstream of the main blade leading edge. It can be seen that while most of the flow was aligned to the axial direction (green color within the black circle), the magnitude of circumferential velocity increased significantly near the shroud side, within the region of 80% span to 100% span. This suggested that the recirculated flow from the ported shroud hardly affected the mainstream flow (below 80% span), but had a large impact on the flow conditions near the impeller tip region, which was also reported in other studies [21]. For the baseline B configuration, the impeller inlet exhibited a negative pre-swirl condition near the shroud side, the mass flow averaged swirl component in this annular region of 80% - 100% span was -11.5 m/s. Whereas for the modified struts M configuration, the impeller inlet had a positive pre-swirl condition with a mass flow averaged swirl component of 29.1 m/s.

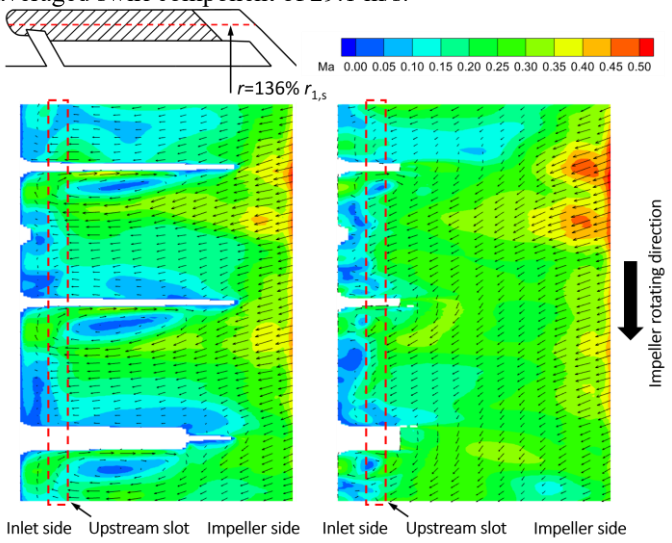

(a) B configuration **(b) M configuration**

Figure 9: Flow field within the annular bleed cavity at normalized *MFP*=0.62 on 100% speedline

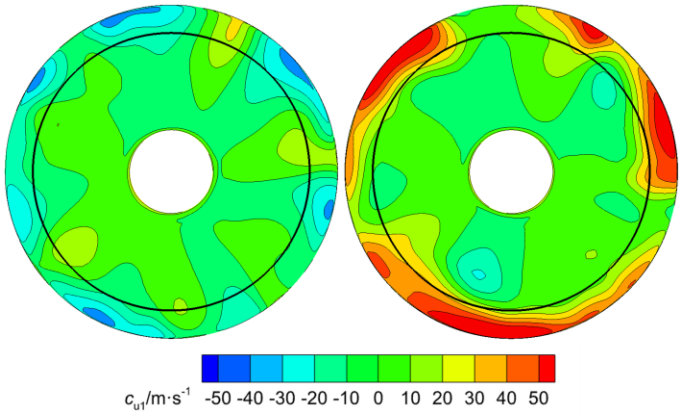

(a) B configuration **(b) M configuration**

Figure 10: Impeller inlet pre-swirl condition at normalized *MFP* = 0.62 on 100% speedline

The mass flow averaged pre-swirl conditions near the impeller tip region (80% span to 100% span) of the different geometry configurations at different speeds are summarized in Figure 11. The circumferential absolute velocity data near tip are normalized by the impeller inlet blade tip speed $u_{1,tip}$ for dimensional consistency. When flow coefficient was greater than 0.33, the tip region had a perfect zero pre-swirl condition. This was because the flow was entering the stage through the ported shroud and bypassing the impeller throat, which was consistent with *RR* characteristic shown in Figure 8. When flow coefficient was less than 0.33, the line of best fit for the pre-swirl condition near the tip region bisected. For the modified struts M configuration, the tip region had a positive pre-swirl condition; for the baseline B and enlarged diffuser recess R configurations, the tip region exhibited negative pre-swirl. The pre-swirl direction aligned with the flow direction of the recirculated flow within the ported shroud cavity shown in Figure 9. It was also

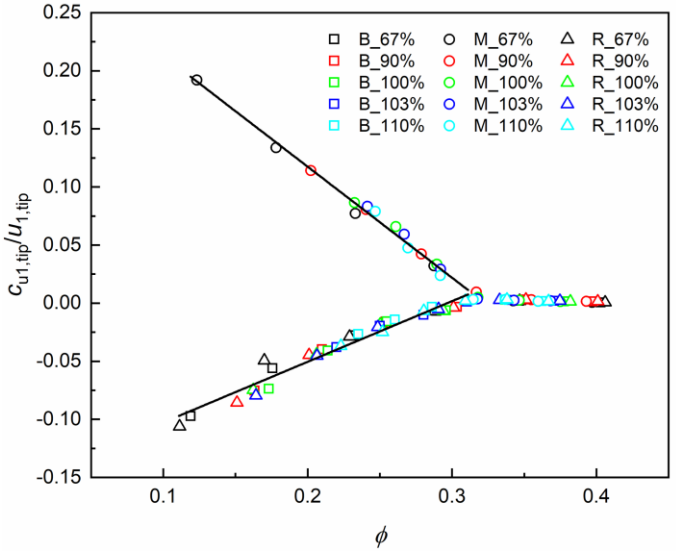

Figure 11: Characteristic of swirl component at impeller inlet near tip region

found that the magnitude of pre-swirl increased linearly with reducing flow coefficient. The range of swirl magnitudes experienced by the baseline B configuration and enlarged recess R configuration was small, at around 50% of that of modified struts M configuration, which aligned with the expectations from Figure 9.

4.3 Modified Impeller Diffusion Factor

Impeller diffusion factor (*DF*) was used to evaluate and quantify the impeller stability in this section. The concept of the *DF* was first introduced by Lieblein [22] in the 1950s. Rodgers [23] then modified this parameter in its application to radial impellers. Historically, this parameter always applied in the preliminary design process to provide an estimation of the impeller stall boundary. In this instance, *DF* has been utilized in conjunction with high-fidelity CFD simulation results to quantify impeller stability and to understand how relative changes to geometry and operating point impact the dominant sub-component governing the location of the last stable operating point of the compressor stage. Hildebrandt et al. [24] has successfully quantified the impeller *DF* with both numerically and experimentally derived data, showing the feasibility of this approach. However, Hildebrandt et al. noticed that relying on 1D spanwise averaging had adverse effects for the *DF* quantification due to nonuniformity of the swirl component. The present paper proposed a modified definition of the *DF* and made improvement to the method for quantifying the *DF*.

Using Rodgers' work as a basis, a novel impeller *DF* was defined that explicitly allowed for including the influence of impeller splitter blades, as shown in Eq. (5):

$$DF = 1 - \frac{w_2}{w_{1,\mathrm{rms}}} + \frac{\pi \cdot r_2}{\left(Z_\mathrm{I} L_\mathrm{I} + Z_\mathrm{E} L_\mathrm{E}\right) \cdot w_{1,\mathrm{rms}}} \left(c_{\mathrm{u}2} - \frac{r_{1,\mathrm{rms}}}{r_2} \cdot c_{\mathrm{u}1} \right) \quad (5)$$

where w_2 is the relative velocity at impeller outlet, $w_{1,\mathrm{rms}}$ is impeller inlet relative velocity at the rms radius. L is the length of the blade and Z is the blade number. The subscripts I and E indicate inducer and exducer. It was assumed that the inducer only had the front part of the main blades, and the exducer had the remaining part of the main blades and all of the splitter blades. $c_{\mathrm{u}1}$ and $c_{\mathrm{u}2}$ are the circumferential components of absolute velocity at impeller inlet and impeller outlet, respectively. The second term of the equation is a diffusion term, which is a variation of De-Haller number, to describe the degree of diffusion of relative velocity within the impeller. The third term is a modification of the Euler turbomachinery equation reflecting the blade-to-blade loading.

According to the results presented in Section 4.2, it can be confirmed that the impeller pre-swirl condition exhibited a clear variation in the spanwise direction. If the impeller pre-swirl was mass flow averaged on a surface encompassing the entire inlet flow area, the impact of the strong pre-swirl condition near impeller tip region on impeller and stage stability would be underestimated. Therefore, the present study separated the impeller in the spanwise direction into the tip region (80% span to 100% span) and the core region (0% span to 80% span), as shown in Figure 12. Impeller *DF* were evaluated separately for the tip region and the core region.

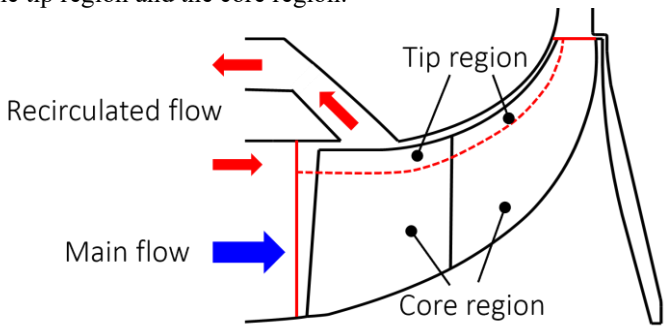

Figure 12: Definition of impeller tip region and core region

Figure 13 shows the impeller *DF* of the tip region and the core region for different geometry configurations at different speeds. Some interesting phenomena can be observed. Impeller *DF* increased with increasing rotating speed, and approached to a critical curve, implying the maximum limit of impeller diffusion. The impeller *DF* of the core region for different geometry configurations overlapped on each speedline (as shown in Figure 13(b)), indicating that the geometry of the ported shroud had little influence on the flow field in the impeller core region, which corresponded to the findings in Figure 10.

When examining the impeller tip region, it was evident that the impeller *DF* of the modified struts M configuration remained lower than that of the baseline B configuration and the enlarged diffuser recess R configuration, except near the choke condition (as shown in Figure 13(a)). The difference became more significant as the flow coefficient decreased. This observation can be attributed to the pre-swirl condition discussed in Section 4.2. The modified struts M configuration provided positive pre-swirl conditions for the impeller tip region, leading to a reduction in the work input in the impeller *DF* formula (third term in Eq. (5)). On the contrary, the baseline B configuration and enlarged recess R configuration introduced a negative pre-swirl condition to the impeller tip region, resulting in an increase in the impeller *DF*. As discussed previously, the third term in Eq. (5) reflects the blade loading. The pre-swirl condition of the impeller tip region actually changes the blade loading and subsequently affects impeller diffusion capability and the stability of compressor stage. This is consistent with previous research [12][13], which highlighted that the positive pre-swirl condition caused by some kinds of ported shroud configurations reduced the blade loading and had a significant influence on compressor stability.

5. DISCUSSION

From the preceding results, it was evident that changes in different geometry configurations had the most pronounced impact on internal flow in the vicinity of impeller tip region. Therefore, the impeller diffusion factors calculated for the impeller tip region are now discussed in more detail. Figure 14 compares the impeller *DF* of the tip region for the three different geometry configurations. It was not possible to obtain a

converged unsteady CFD result for the last experimentally stable operating point of the enlarged diffuser recess R configuration at 103% speed. Thus, the impeller *DF* value at this operating point was extrapolated based on the impeller *DF* values of other operating points on the same speedline, marked as a solid triangle in Figure 14(c).

For the baseline B configuration, the impeller demonstrated the ability to achieve a high and constant limiting *DF* value (~0.86) when approaching the surge limit at the speedlines of 67%, 90% and 100%. This implied that the stage instability was primarily influenced by the impeller at these conditions, in other words, the impeller could not work stably at a higher *DF* value than this. Also, this suggested that the impeller had become the dominant component of the instability of the whole compressor stage. When the compressor was accelerated to higher speedlines of 103% and 110%, it can be observed that the limiting *DF* value decreased significantly at the surge boundary. There would be two explanations for this. One possibility was that the impeller internal flow field changed, such as the presence of shock waves,

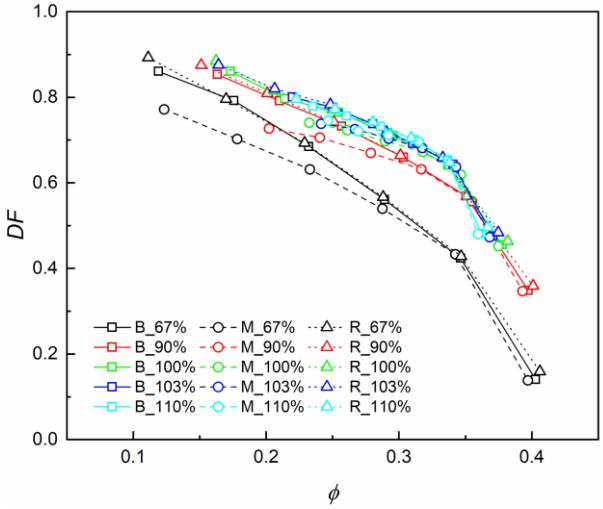

(a) *DF* at tip region

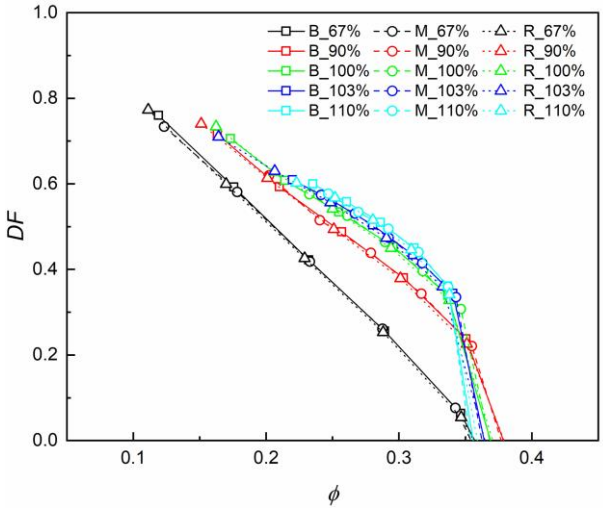

(b) *DF* at core region

Figure 13: Impeller diffusion factor (*DF*) at tip region and core region

leading to the decrease of limiting *DF*. However, no shock waves were observed through CFD results. Thus, it could be inferred that something happened in other components decreased the impeller limiting *DF*. It was presumed that the diffuser potentially stopped the impeller from reaching its maximum *DF* value, since diffuser instability triggered compressor surge at higher flow rates than the impeller could tolerate. This indicated that the instability of the whole compressor stage had shifted to being dominated by the diffuser rather than the impeller.

Figure 15 presents instantaneous unsteady CFD results to demonstrate and characterize the dominant flow structures contributing to the transition from impeller dominated stall to diffuser dominated stall, linking to the insight generated by the *DF* analysis. The near surge conditions of two typical shaft speeds (100%: impeller dominated stall; 110%: vaneless diffuser dominated stall) at 90% span were compared. Entropy generation rate (s_g) [25] normalized by the inducer tip velocity was adopted to show the extent of flow losses and dominant flow structures. At the near surge condition for 100% speedline, high s_g areas can be observed after the downstream slot of the ported shroud (region ①), appearing in almost all blade passages and extending across each blade passage. This indicated that the instability within the impeller was pronounced at this operating point. At 110% speed, the high s_g areas at region ① disappeared, leaving relatively uniform flow within the inducer blade passages. However, high s_g areas exhibiting increased intensity were observed in the diffuser (region ②), and a more prominent high s_g area developed near the volute tongue. This suggested that the instability within the impeller was no longer dominant, and the flow losses within the diffuser exerted a more significant impact on stage instability.

Similar phenomena can be observed in the *DF* curves of the modified struts M configuration and the enlarged diffuser recess R configuration. The difference existed in the switch over between the dominant instability components was at lower speeds (67%-90%) for the modified struts M configuration, and at higher speeds (103%-110%) for the enlarged diffuser recess R configuration. This switch over of the dominant instability component is also reflected in the kink on the compressor performance map (see Figure 3).

The value of high limiting impeller *DF* noted in Figure 14 clearly shows that the enlarged diffuser recess R configuration had improved impeller stability, as the increased limiting impeller *DF* value indicated that the impeller could stably operate with a greater degree of flow diffusion. Taking the limiting impeller *DF* as an indicator of impeller stability, the enhancement of impeller stability due to the enlarged diffuser recess was about 3%. By contrast, the reduced axial extent of the modified struts in the M configuration had weakened the impeller stability. The impeller stability of the modified strut M configuration was only 90% of that of the baseline B configuration.

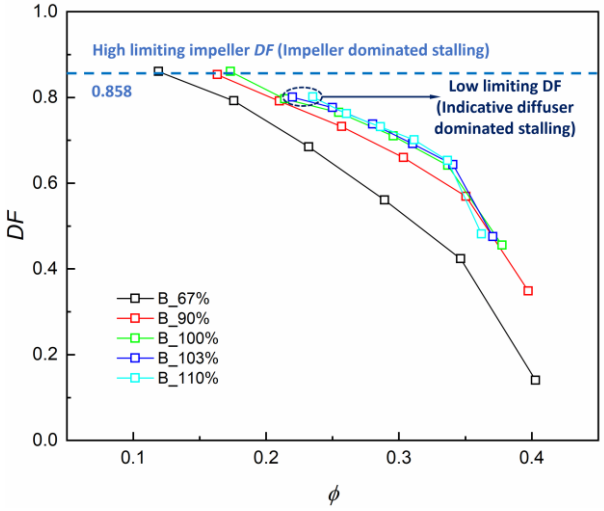

(a) Baseline B configuration

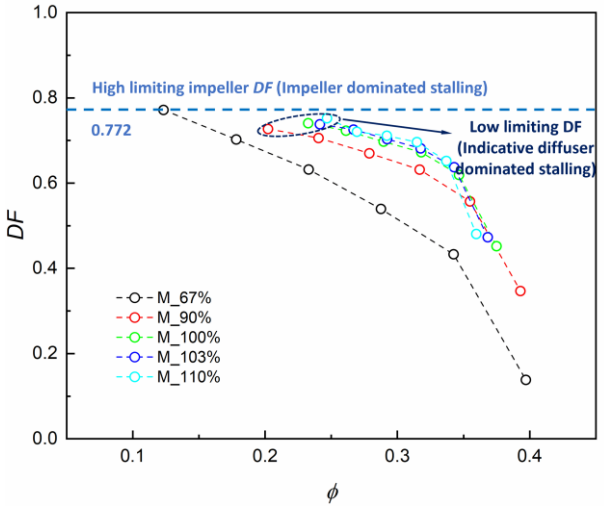

(b) Modified struts M configuration

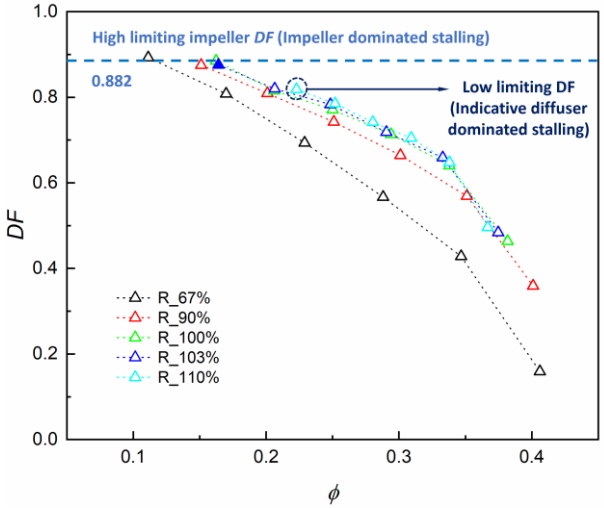

(c) Enlarged recess R configuration

Figure 14: Impeller diffusion factor (*DF*) at tip region for different geometry configurations

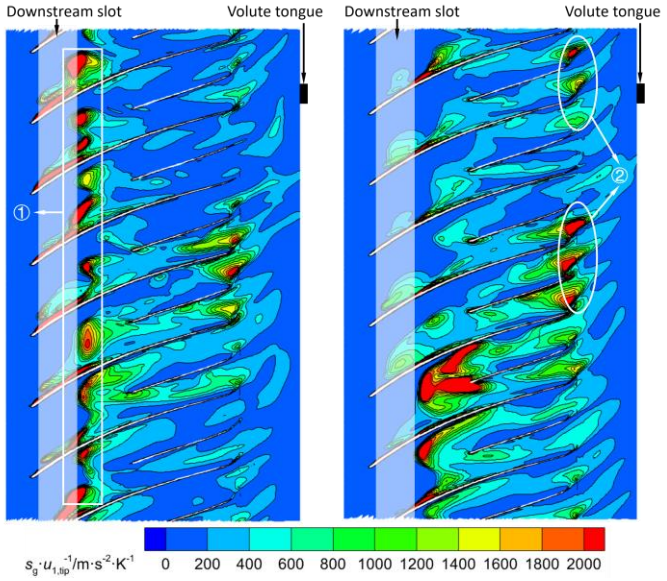

(a) B_100% **(b) B_110%**

Figure 15: Normalized entropy generation rate at 90% span for the near surge operating point (Baseline configuration)

Stall lines of impeller and vaneless diffuser for different geometry configurations based on limiting impeller *DF* values were correlated with known experimentally measured surge boundary, and were illustratively represented in Figure 16, overlaid with the compressor performance map. The dashed lines and the double dashed lines represent vaneless diffuser stall and impeller stall, respectively. In the case of the baseline B configuration, the impeller stall line had a steeper slope than that of vaneless diffuser stall line, which was in line with the findings reported by Jansen et al. [26]. The difference in the slopes between impeller stall line and vaneless diffuser stall line resulted in the dominant instability at lower speeds being due to the impeller component. The switch over of instability dominant component happened when the two stall lines intersected, somewhere between 100% and 103% speed.

The situation for the enlarged diffuser recess R configuration was similar. However, since the enlarged diffuser recess improved the impeller stability to a certain extent, it shifted the impeller stall line slightly to the left. Additionally, the enlarged diffuser recess also enhanced diffuser stability, as pointed by Nikpour [10], pushing the vaneless diffuser stall line significantly up and to the left.

For the modified struts M configuration, the decreased limiting impeller *DF* value corresponded to a reduction in impeller stability, which was caused by the positive pre-swirl at impeller tip region. This moved the impeller stall line to the right. In addition, the deteriorated impeller also reduced the stability of the downstream diffuser, resulting in the vaneless diffuser stall line moving to the right. Furthermore, the slopes of impeller stall line and the vaneless diffuser stall line were remarkably similar. This led to little variation in the limiting impeller *DF* values at high speeds, irrespective of whether the compressor instability was dominated by the impeller or the vaneless diffuser.

Consequently, the surge limit of the modified struts M configuration had no obvious kink.

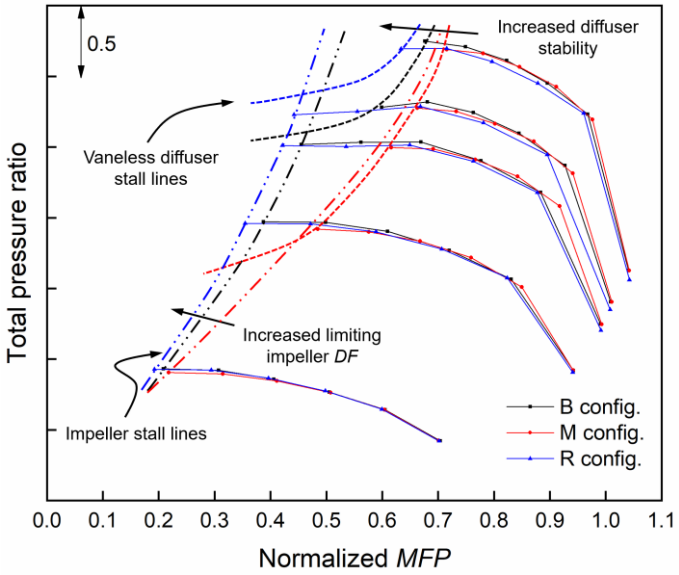

Figure 16: Schematic of stall lines of compressor sub-components

6. CONCLUSIONS AND FUTURE WORK

The stability of a ported shroud turbocharger compressor stage with various geometry configurations has been investigated. A high-fidelity CFD model was established to obtain fundamental understanding of the compressor flow field for three different geometry configurations. To faithfully replicate the experimentally tested compressor stage and obtain accurate flow field predictions, particular techniques were included in the modelling strategy, such as preserving geometry details, carefully defining interfaces, and manually generating a structured grid for the impeller domain. Based on the knowledge of flow analysis from numerical simulation results, the impeller diffusion factor was modified and applied to analyze the variation in compressor stage stability. The following conclusions can be drawn from the results of the study:

1. The recirculated flow from the ported shroud only affected the flow in the upper 20% of the span at the impeller tip region. The proportion of recirculated flow was a quartic function of the stage flow coefficient and increased as stage flow coefficient reduced.
2. The struts of the baseline ported shroud device created a negative pre-swirl condition for the impeller inlet tip region, whereas the shorter struts for a modified ported shroud configuration generated a positive pre-swirl condition at the impeller inlet tip region. The magnitude of swirl component was found to increase linearly with the reduction in stage flow coefficient.
3. A modified calculation for impeller diffusion factor (*DF*) was proposed to include the effect of splitter blades, which calculated the value focused at the outer span region near the tip where the flow was impacted by the recirculated swirling flow. The modified impeller *DF* value at the tip region provided a consistent reference boundary for impeller instability.
4. A shift in the value of the limiting impeller diffusion factor (*DF)* indicated that the dominant component of compressor instability switched from impeller stall to vaneless diffuser stall at higher speeds.
5. Based on the limiting impeller diffusion factor (*DF)* values, the impeller stability of different geometry configurations was quantified. Combined with the stage performance map, it was found that the modified struts M configuration decreased the impeller stability by 10% and also deteriorated the stability of the downstream diffuser. The enlarged diffuser recess R configuration improved not only the diffuser stability, but also enhanced the impeller stability by 3%.

The novelty of this work is the improvement of the impeller diffusion factor and its evaluation method, according to the impact of the ported shroud on the internal flow field. The developed method and the results presented provide a reference for the application of a traditional 1D performance metric derived from 3D CFD simulations, and hence gaining an understanding of how geometry configuration changes affect impeller stability and the whole stage stability. Future work will focus on stability mechanism analysis, to clearly understand the principles of compressor stability change caused by different geometry configurations, and to characterize the changes to the internal flow field associated with compressor surge inception.

ACKNOWLEDGEMENTS

The authors gratefully acknowledge Cummins Engine Components for providing research support and permission to publish this work. Acknowledgement is extended to Irish Centre for High-End Computing (ICHEC) for the provision of computational facilities and support, and to Ansys Inc for the use of their software. The author would also like to thank China Scholarship Council (No. 202006280008) for financially supporting Yiming Liu's PhD study at Trinity College Dublin.

REFERENCES

[1] Stuart, C., Spence, S., Teichel, S., and Starke, A., 2021, "Experimental and Numerical Assessment of the Impact of an Integrated Active Pre-Swirl Generator on Turbocharger Compressor Performance and Operating Range," Energies, **14**(12), p. 3537.

[2] Fisher, F. B., 1988, "Application of Map Width Enhancement Devices to Turbocharger Compressor Stage," SAE Technical Paper No. 880794.

[3] Sivagnanasundaram, S., Spence, S., Early, J., and Nikpour, B., 2013, "An Impact of Various Shroud Bleed Slot Configurations and Cavity Vanes on Compressors Map Width and the Inducer Flow Field," ASME J. Turbomach., **135**(7), p. 041003.

[4] Sivagnanasundaram, S., Spence, S., and Early, J., 2014, "Map Width Enhancement Technique for a Turbocharger Compressor," ASME J. Turbomach., **136**(6), p. 061002.

[5] Tamaki, H., Zheng, X., and Zhang, Y., 2013, “Experimental Investigation of High Pressure Ratio Centrifugal Compressor With Axisymmetric and Nonaxisymmetric Recirculation Device,” ASME J. Turbomach., **135**(3), p. 031023.
[6] Yang, M., Zheng, X., Zhang, Y., Bamba, T., Tamaki, H., Huenteler, J., and Li, Z., 2013, “Stability Improvement of High-Pressure-Ratio Turbocharger Centrifugal Compressor —Part I: Non-Axisymmetrical Flow in Centrifugal Compressor,” ASME J. Turbomach., **135**(3), p. 021006.
[7] Zheng, X., Zhang, Y., Yang, M., Bamba, T., and Tamaki, H., 2013, “Stability Improement of High-Pressure-Ratio Turbocharger Centrifugal Compressor by Asymmetrical Flow Control—Part II: Nonaxisymmetrical Self-Recirculation Casing Treatment,” ASME J. Turbomach., **135**(3), p. 021007.
[8] He, X., and Zheng, X., 2019, “Roles and Mechanisms of Casing Treatment on Different Scales of Flow Instability in High Pressure Ratio Centrifugal Compressors,” Aerosp. Sci. Technol., **84**(2019), pp. 734-746.
[9] Guillou, E., Gancedo, M., and Gutmark, E., 2016, “Experimental Investigation of Flow Instability in a Turbocharger Ported Shroud Compressor,” ASME, J. Turbomach., **138**(6), p. 061002.
[10] Nikpour, B., 2004, “Turbocharger Compressor Flow Range Improvement for Future Heavy Duty Diesel Egnines,” THIESEL 2004 Conference on Thermo- and Fluid Dynamic Processes in Diesel Engines, Valencia, Spain, September 7-10.
[11] Spakovszky, Z. S., and Roduner, C. H., 2009, “Spike and Modal Stall Inception in an Advanced Turbocharger Centrifugal Compressor,” ASME J. Turbomach., **131**(7), p. 031012.
[12] Chen, H., and Lei, V-H., 2013, “Casing Treatment and Inlet Swirl of Centrifugal Compressors,” ASME J. Turbomach., **135**(4), p. 041010.
[13] Tamaki, H., 2012, “Effect of Recirculation Device With Counter Swirl Vane on Performacne of High Pressure Ratio Centrifugal Compressor,” ASME J. Turbomach., **134**(5), p. 051036.
[14] SAE, 1995, “Turbocharger Gas Stand Test Code,” Society of Automotive Engineers, Warrendale, PA, Standard No. J1826_199503.
[15] Whittlesea, M., and Roberts, E., 2016, “Turbo Charger Compressor Inlet and Outlet Pipe Length and Volume, and the Effects on the Characteristics and Location of Surge,” 12th International Conference on Turbochargers and Turbocharging, May 17-18, London, IMechE, Paper No. 4.
[16] Vahdati, M., Sayma, A. I., Freeman, C., and Imregun, M., 2005, “On the Use of Atmospheric Boundary Conditions for Axial-Flow Compressor Stall Simulations,” ASME J. Turbomach., **127**(2), pp. 349-351.
[17] Galloway, L., Rusch, D., Spence, S., Vogel, K., Hunziker, R., and Kim, S, i., 2018, “An Investigation of Centrifgual Compressor Stability Enhancement Using a Novel Vaned Diffuser Recirculation Technique,” ASME J. Turbomach., **140**(12), p. 121009.
[18] Celik, I. B., Ghia, U., and Roache, P. J., 2008, “Procedure for Estimation and Reporting of Uncertainty due to Discretization in CFD Applications,” ASME J. Fluid Eng., **130**(7), p. 078001.
[19] Richardson, L. F., 1910, “The Approximate Arithmetical Solution by Finite Differences of Physical Problems Involving Differential Equations, with an Application to the Stresses In a Masonary Dam,” Transaction of the Royal Society of London, Ser. A, Vol. 210, pp. 307-357.
[20] Yang, F., Wu, Y., Chen, Z., Spence, S., and Li, B., 2023, “The Unsteadiness of Tip Leakage Vortex Breakdown and Its Role in Rotating Instability,” Phys. Fluids, **35**(2023), p. 107107.
[21] Cravero, C., Leutcha, P. J., and Marsano, D., 2022, “Simulaton and Modeling of Ported Shroud Effects on Radial Compressor Stage Stability Limits,” Energies, **15**(7), p. 2571.
[22] Lieblein, S., 1965, “Experimental Flow in Two-Dimensional Cascades,” Aerodynamic Design of Axial-Flow Compressors. NASA SP-36, ch. 6.
[23] Rodgers, C., 1978, “A Diffusion Factor Correlation for Centrifugal Impeller Stalling,” ASME J. Eng. Power, **100**(4), pp. 592-601.
[24] Hildebrandt, A., Ceyrowsky, T., Klausmann, J., and Metz, K. A., 2022, “On the Correlation Between Spanwise Inducer Incidence and Impeller Diffusion for Ruled Surface and Barreled Sweep-Bow Impeller Design at Inlet Guide Vane-Off-Design,” ASME J. Turbomach., **144**(2), p. 021005.
[25] Newton, P., Palenschat, T., Martinez-Botas, R., and Seiler, M., 2015, “Entropy Generation Rate in a Mixed Flow Turbine Passage,” International Gas Turbine Congress (IGTC), Tokyo, Japan, Nov. 15-20, pp. 911-920.
[26] Jansen, J., Carter, A. F., and Swarden, M. C., 1980, “Improvements in Surge Margin for Centrifugal Compressors,” AGARD conference proceedings, No. 282, pp. 19.1-19.16.